Time-Frequency Duality of Biphotons for Quantum Optical Synthesis

Rui-Bo Jin,[1] Takuma Saito,[2] and Ryosuke Shimizu[2,*]

[1] *Laboratory of Optical Information Technology, Wuhan Institute of Technology, Wuhan 430205, China*
[2] *The University of Electro-Communications, 1-5-1 Chofugaoka, Chofu, Tokyo, Japan*

(Received 7 December 2017; revised manuscript received 4 April 2018; published 7 September 2018)

Time-frequency duality, which enables the control of optical waveforms by manipulating the amplitudes and phases of electromagnetic fields, plays a pivotal role in a wide range of modern optics. The conventional one-dimensional (1D) time-frequency duality has been successfully applied to characterize the behavior of classical light, such as ultrafast optical pulses from a laser. However, the 1D treatment is not enough to characterize quantum-mechanical correlations in the time-frequency behavior of multiple photons, such as the biphotons from parametric down-conversion. Two-dimensional (2D) treatment is essentially required, but has not been fully demonstrated yet due to technical problems. Here, we study the 2D time-frequency duality of biphotons, by measuring two-photon distributions in both the frequency and the time domain. It is discovered that the generated biphotons satisfy the Fourier-transform-limited conditions in a two-photon spectral distribution, but do not satisfy those conditions in the single-photon marginal distribution. Our study may pave the way for the quantum-optical synthesizer, the next-generation technology beyond the traditional optical synthesis in the time-frequency domain.

DOI: 10.1103/PhysRevApplied.10.034011

I. INTRODUCTION

Optical studies that utilize the relationship coupled by the Fourier transform are called Fourier optics, and form a wide range of optical-science and -technology fields, including optical imaging [1–3], spectroscopy [4,5], optical measurement [6,7], and optical signal processing [8,9]. In particular, it is well known that each electric-field distribution in the time and frequency domains is connected by the one-dimensional Fourier transform (1DFT)

$$A^{(1)}(t) = \frac{1}{\sqrt{2\pi}} \int d\nu \tilde{A}^{(1)}(\nu) e^{-2\pi i \nu t}, \tag{1}$$

where $A^{(1)}(t)$ is the electric-field amplitude as a function of time t, and $\tilde{A}^{(1)}(\nu)$ is the corresponding distribution with a frequency ν, as shown in Fig. 1(a). This relationship is a fundamental principle of cutting-edge technologies on an ultrashort pulse laser, as seen in the recent developments in optical synthesis [10,11]. On the other hand, Fourier optical phenomena can also be explained from the viewpoint of the particle nature of light, i.e., the photon. The photons contained in a laser light pulse have no quantum correlation, which can be understood in relation to the phenomenon that a single-photon state has the same interference pattern as a coherent state in a Young's double-slit experiment. Therefore, the collective behavior of a many-photon system can be handled as a single-photon problem [12,13]. As a result, the quantum-mechanical treatment between the time and frequency domains of a laser light pulse can be explained by 1DFT, producing results corresponding to an understanding of classical wave optics. However, in principle, these phenomena should be treated as a quantum many-body system, because a large number of photons are contained in an optical pulse output from an ultrashort pulse laser.

Recent progress in quantum-optical technologies allows us to control not only a number of photons (i.e., photon statistics), but also the frequency-related quantum correlations in an optical pulse [14–17]. Such a frequency quantum correlation would affect its temporal distribution directly through time-frequency duality. It is not reasonable to treat the behavior of a quantum-mechanically-correlated photon as a single-photon (or 1D) problem. Therefore, an optical pulse containing the correlated photons requires a higher-order Fourier treatment that incorporates the quantum mechanics. As the first step toward future photonics at the single-photon level in the time-frequency domain, we focus here on the time-frequency behavior of biphotons, which requires the treatment of the two-dimensional Fourier transform (2DFT), as shown in Figs. 1(b) and 1(c).

$$A^{(2)}(t_1, t_2) = \frac{1}{2\pi} \int \int d\nu_1 d\nu_2 \tilde{A}^{(2)}(\nu_1, \nu_2) e^{-2\pi i(\nu_1 t_1 + \nu_2 t_2)}, \tag{2}$$

*r-simizu@uec.ac.jp

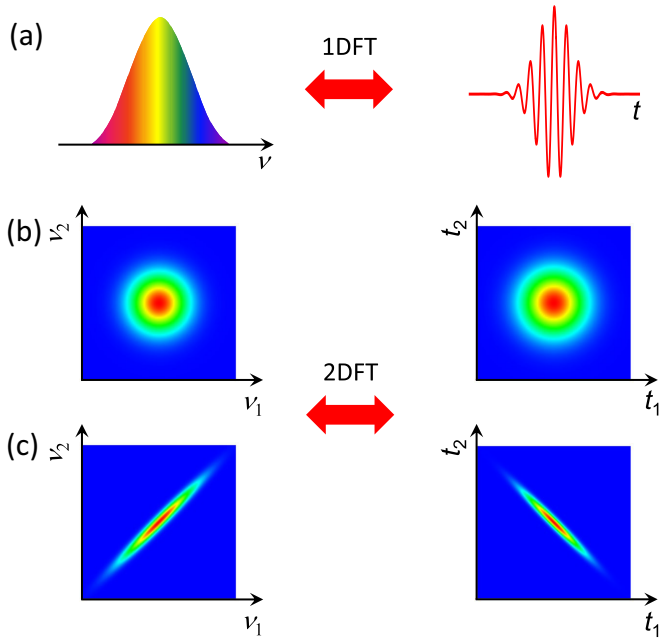

FIG. 1. A conceptual drawing of 1D and 2D treatments for the time-frequency duality. (a) Classical duality in the time-frequency domain; a broader distribution in the frequency domain results in a narrower distribution in the time domain. (b) A 2D Fourier transform for a frequency-uncorrelated biphoton; frequency uncorrelation leads to uncorrelation in the time domain. (c) A 2D Fourier transform of a biphoton with positive frequency correlation; correlations are inverted between the time and frequency domains.

where $A^{(2)}(t_1, t_2)$ is the biphoton probability amplitude at time t_1 and t_2, and $\tilde{A}^{(2)}(\nu_1, \nu_2)$ is the corresponding distribution with the frequencies ν_1 and ν_2.

From the early stage of quantum-optical experiments, the time-frequency correlation of biphotons generated from spontaneous parametric down-conversion processes has been investigated extensively [18–30]. In these studies, the authors have discussed the relationship between a classical frequency spectrum and time-domain quantum interference patterns [19–23], the spectral properties [24–27], or the temporal [28–30] properties of biphotons. These studies provide a partial understanding of the nonclassical behavior of biphotons. However, it is necessary to consider the 2D time-frequency space for a comprehensive understanding of biphoton behavior, but this still has not been fully demonstrated due to technical problems. Here, we experimentally demonstrate the time-frequency duality of biphotons with positive frequency correlation, by measuring both the two-photon spectral intensity distribution (TSI) and the two-photon temporal intensity distribution (TTI). Furthermore, we show the variation of two-photon temporal distributions as a result of two-photon spectral modulations, retaining quantum-optical Fourier-transform-limited conditions.

II. RESULTS

To generate biphotons with positive frequency correlation, we exploit the spontaneous parametric down-conversion process in a periodically poled potassium titanyl phosphate (PPKTP) crystal pumped by a mode-locked titanium sapphire laser, operating at a center wavelength of 792 nm. Thanks to the group-velocity matching condition [31,32] with the femtosecond-laser-pulse pumping, we could generate biphotons with positive frequency correlation at a center wavelength of 1584 nm (see the Appendix for details). Since biphotons generated via the type-II phase-matching condition have orthogonal polarizations, the polarization of the constituent photons is aligned along either the crystallographic y or z axis. To manipulate a two-photon spectral distribution, we use pump pulses with a bandwidth of either 8.1 or 2.8 nm. In addition, we prepare two PPTKP crystals, one 30 mm and the other 10 mm long, and position one or the other in our experimental apparatus (see the Appendix).

We perform two experiments to characterize the biphoton distributions in the time-frequency domain. A two-photon spectrometer consisting of two tunable bandpass filters, which has a Gaussian-shaped filter function with a fixed full width at half maximum (FWHM) of 0.56 nm, and a tunable central wavelength from 1560 to 1620 nm, followed by a two-photon detector, enable us to conduct the TSI measurements [25,32]. For the TTI measurements, we utilize a time-resolved up-conversion detection system with a spatial multiplexing technique [29,33]. We measure the TTI by scanning the temporal delay between the constituent photons and the local oscillator pulse coming from the mode-locked laser with a step length of 0.13 ps, and we record the coincidence events (see the Appendix).

Figure 2 shows the experimentally measured TSIs (left) and TTIs (right) with a combination of the two different pump bandwidths (2.8 or 8.1 nm) and two different crystal lengths (10 or 30 mm). We reproduce TSIs and TTIs deconvoluted from the original data, taking into account the resolutions of our two-photon detection systems (see the Appendix). In Fig. 2, the horizontal (vertical) axis $\Delta\nu_y$ ($\Delta\nu_z$) is the frequency shift from the center frequency of each distribution in the photons polarized in the y (z) directions. The zero-shifted frequency is 189.4 THz, corresponding to a center wavelength of 1584 nm. The specific features of the time-frequency duality of the biphotons can be clearly observed in Fig. 2; the TSI of the biphotons from the PPKTP crystal has a positively correlated distribution along the diagonal ($\Delta\nu_y = \Delta\nu_z$) direction, while the corresponding TTI has a negatively correlated distribution along the antidiagonal ($\Delta\nu_y = -\Delta\nu_z$) direction.

When the pump bandwidth is increased from 2.8 nm in Fig. 2(a) to 8.1 nm in Fig. 2(b) for the fixed crystal length of 30 mm, the TSI becomes slightly broader along the diagonal direction, while the width is unchanged

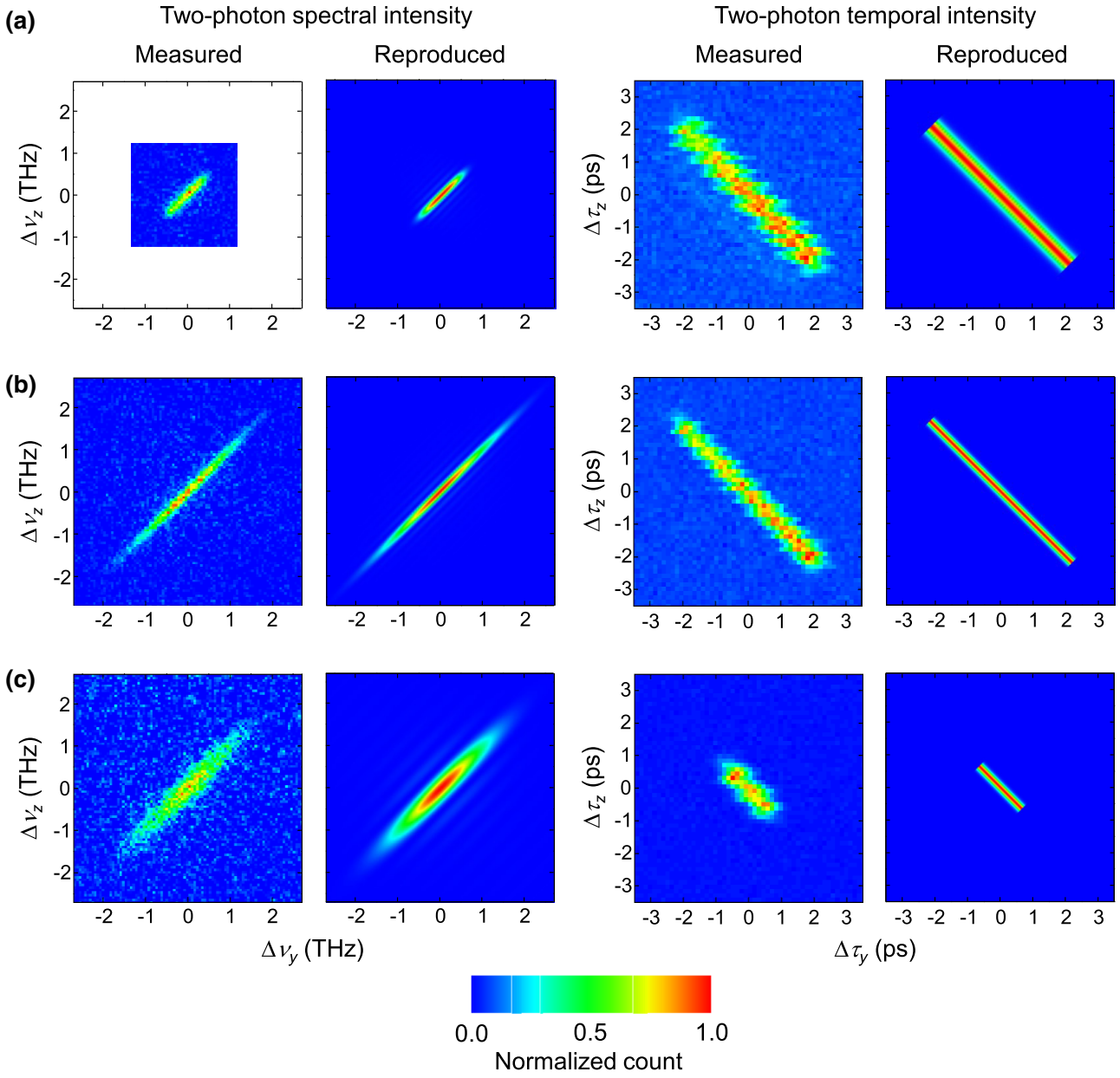

FIG. 2. Observation of the time-frequency duality of biphotons. The plots in the two columns on the left are the TSIs, and those in the two columns on the right are the TTIs. No measurements are carried out in the white area in (a). The biphotons are produced under different conditions. (a) The pump has a near-rectangular profile with a bandwidth $\Delta\lambda_p$ of 2.8 nm and a PPKTP crystal length L of 30 mm; (b) The pump has a Gaussian profile with a bandwidth $\Delta\lambda_p$ of 8.1 nm and a length L of 30 mm; (c) The pump also has a Gaussian profile with a bandwidth $\Delta\lambda_p$ of 8.1 nm and a length L of 10 mm. The temporal distributions are varied by manipulating the spectral distributions.

along the antidiagonal direction. In the same manner, when the crystal length L is shortened from 30 mm in Fig. 2(b) to 10 mm in Fig. 2(c), the TSI becomes broader along the antidiagonal direction, while staying the same in the diagonal direction. We can understand these phenomena in view of the following facts: the biphoton spectral amplitude $\tilde{A}^{(2)}(\Delta\nu_y, \Delta\nu_z)$ is the product of a phase-matching function $\Phi(\nu_-, L)$ and a pump spectral function $\alpha(\nu_+)$; $\tilde{A}^{(2)}(\nu_+, \nu_-) = \Phi(\nu_-, L)\alpha(\nu_+)$, where $\nu_\pm = \frac{1}{\sqrt{2}}(\Delta\nu_y \pm \Delta\nu_z)$ and L is the given PPKTP length. Therefore, the bandwidth of the TSI in the ν_+ direction is determined by the spectral function of the pump laser, while that in the ν_- direction is determined by the phase-matching function, which depends on the crystal length L (see the Appendix). Thus, in our case, the time-frequency duality of the biphoton can be expressed in the

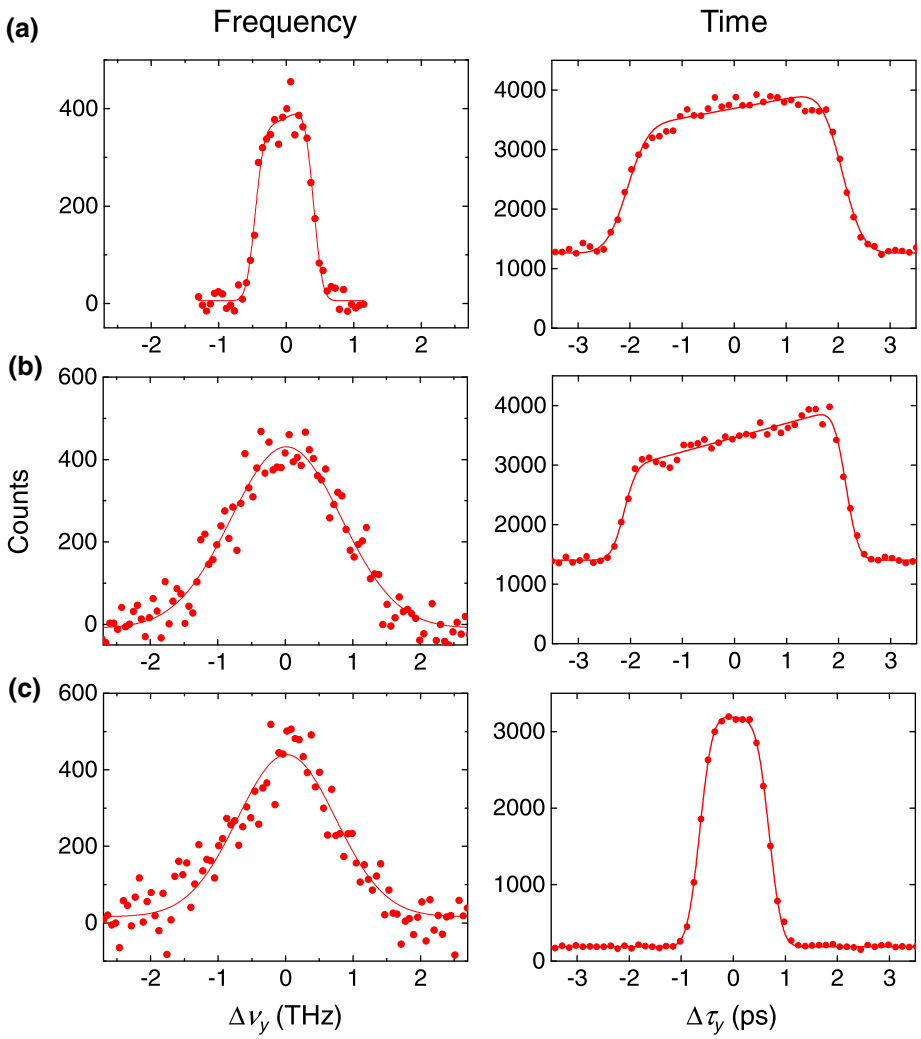

FIG. 3. The marginal distributions of the two-photon spectral- and temporal-intensity distributions. The graphs on the left are the marginal distributions of the TSIs, shown in Fig. 2, projecting onto the $\Delta\nu_y$ axis. The graphs on the right are those of the TTIs, projecting onto the $\Delta\tau_y$ axis. The red lines represent a least-squares fit to the data. Background counts exist in the TTI measurements due to the unwanted photon-pair generation in the up-conversion crystal. No relations are observed for corresponding distributions between the time and frequency domains.

following form:

$$A^{(2)}(\Delta\tau_y,\Delta\tau_z) = \frac{1}{\sqrt{2\pi}}\int d\nu_+\alpha(\nu_+)e^{-2\pi i\nu_+\tau_+} \times \frac{1}{\sqrt{2\pi}}\int d\nu_-\Phi(\nu_-,L)e^{-2\pi i\nu_-\tau_-} = A_1^{(1)}(\tau_+)A_1^{(1)}(\tau_-), \quad (3)$$

where $\tau_\pm = \frac{1}{\sqrt{2}}(\Delta\tau_y \pm \Delta\tau_z)$. This indicates that the 2DFT can be decomposed into the product of two 1DFTs: $A_1^{(1)}(\tau_+) = (1/\sqrt{2\pi})\int d\nu_+\alpha(\nu_+)e^{-2\pi i\nu_+\tau_+}$ and $A_2^{(1)}(\tau_-) = (1/\sqrt{2\pi})\int d\nu_-\Phi(\nu_-,L)e^{-2\pi i\nu_-\tau_-}$. Based on this, we can confirm the time-bandwidth product (TBP) between $\delta\tau_+$ and $\delta\nu_+$, or $\delta\tau_-$ and $\delta\nu_-$, where $\delta\tau_\pm$ ($\delta\nu_\pm$) are the FWHM values along the $\tau_\pm$ ($\nu_\pm$) directions in the TTIs (the TSIs).

Using the data reproduced in Fig. 2, we estimate $\delta\nu_\pm$ and $\delta\tau_\pm$ for all the cases in Fig. 2 and calculate the TBPs. It is worth evaluating the TBPs for the marginal distributions, as shown in Fig. 3, because they can be observed by classical spectroscopic measurements. Here, $\delta\nu_y(\delta\tau_y)$ is the FWHM of the marginal distribution of the TSI (TTI) after the deconvolution. All of the TBP values are summarized in Table I.

It is obvious that the TBP values between $\delta\tau_\pm$ and $\delta\nu_\pm$ are less than 1, meaning that the generated biphoton wave packets satisfy the nearly Fourier-transform-limited conditions. The values of $\delta\nu_+ \times \delta\tau_+$ are almost determined by the pump-pulse spectra $\alpha(\nu_+)$, and would have a value of approximately 0.44 when assuming a Gaussian distribution. On the other hand, $\delta\nu_- \times \delta\tau_-$ is associated with the phase-matching function $\Phi(\nu_-,L)$, and the values would be approximately 0.87 due to the rectangular shape of the PPKTP crystals along the propagation direction of the pump pulse. However, the value of $\delta\nu_y \times \delta\tau_y$ in Table I is clearly larger than 1. This implies that the constituent photons of the biphoton wave packet no longer satisfy the Fourier-transform-limited conditions (i.e., the coherence of the single-photon wave packets is degraded). The disappearance of the single-photon coherence is an inherent characteristic in a quantum-mechanical biparticle system and is well known as the degradation of purity in

TABLE I. Time-bandwidth products of the biphoton wave packets. A summary of the time-bandwidth products in three experimental conditions in Fig. 2. All the values are less than 1 in the two-photon distributions, implying that biphotons nearly satisfy the Fourier-transform-limited conditions. On the other hand, the time-bandwidth product values in the marginal distributions clearly do not meet the Fourier-transform-limited conditions.

	$\Delta\lambda_p$ (nm)	L (mm)	$\delta\tau_+ \times \delta\nu_+$	$\delta\tau_- \times \delta\nu_-$	$\delta\tau_y \times \delta\nu_y$
a	2.8	30	0.46	0.77	3.4
b	8.1	30	0.49	0.85	8.2
c	8.1	10	0.41	0.59	2.2

a qubit system [34], or a complementary relationship in position-momentum entangled states [35,36].

III. DISCUSSION

We now consider the difference in time-frequency duality between the classical and quantum regimes. It is known that the Hamiltonian for a classical electromagnetic wave can be written as the sum of Hamiltonians for independent harmonic oscillators. Thus, in terms of the photon picture, we can interpret classical optical phenomena as the collective behavior of uncorrelated photons, which results in a single-photon (1D) treatment. Under the 1D treatment, we understand that the electric-field amplitude, or the one-photon probability amplitude, between the time and frequency domains are conjugate physical quantities. In contrast, the limitation of the 1D treatment is evident from the results presented in Figs. 2 and 3. In practice, the TBP of $\delta\nu_y \times \delta\tau_y$ implies that the single-photon spectrum associated with the marginal distribution in the frequency domain is no longer conjugate with the single-photon temporal shape. In our case, it is obvious that the marginal distribution in the frequency domain is mostly determined by the distribution along the diagonal direction in the TSIs, whose Fourier conjugate pair is the distribution along the diagonal direction in the time domain. In other words, the single-photon spectral distribution strongly affects the temporal quantum correlation of the biphoton. In the same manner, the frequency quantum correlation leads to the single-photon temporal distribution. Through these considerations, we can understand classical optical theory is applicable only for the collective behavior of uncorrelated photons such as laser pulses. Higher-order treatments that incorporate the quantum mechanics, such as a quantum many-body system [37], are essentially required for a general understanding of the nature of light.

This study on the biphoton system is the starting point for investigations of a multiphoton (many-body bosonic) system. In fact, the three-photon temporal correlations have been measured recently [38,39]. Based on the technology in this work, it is possible to measure the joint spectral distributions and joint temporal distributions of the three-or-more-photon state in the future. Our study opens up possible alternative directions for optical science and technology, taking into account the quantum correlation, which classical optics treats as the collective motion of uncorrelated photons. Specifically, time-frequency duality with higher-dimensional treatments has great potential to manage a multiple-photon wave packet in a higher-dimensional time-frequency space.

One possible application of our experiment is quantum-optical synthesis, which will be the next-generation technology beyond traditional optical synthesis [10,11]. Complete control of light fields has been a major challenge in optical science and engineering. Recent developments in laser technology allow us to control not only the shape of the temporal envelope but also the carrier-envelope phase in an optical pulse by manipulating the phase and amplitude of the discrete frequency modes. Such optical synthesis is technologically sophisticated, but the basic theory is very simple: one-dimensional Fourier transforms between the time and frequency domains. In contrast, the control of quantum correlations of photons, which is the most striking feature of a multiphoton wave packet, is of great interest in quantum-optical fields and is being developed together with quantum information technologies. By integrating conventional optical synthesis with quantum-optical technologies, this work may pave the way for creating an arbitrary waveform of the multiphoton wave packet in a high-dimensional time-frequency space.

IV. CONCLUSION

In summary, we demonstrate the correlation inversion between the time and frequency domains for biphotons with positive frequency correlation, by experimentally measuring two-photon distributions in both domains. It is discovered that the generated biphotons satisfy the Fourier-transform-limited conditions quantum mechanically (i.e., in the two-photon spectral distribution), but not classically (i.e., in the single-photon marginal distribution). Our study opens up possible alternative directions for optical science and technology with a many-body system and in a high-dimensional frequency space, such as the technology of quantum-optical synthesis.

In fact, our study also involves the direct observation of energy-time-entangled photon pairs.

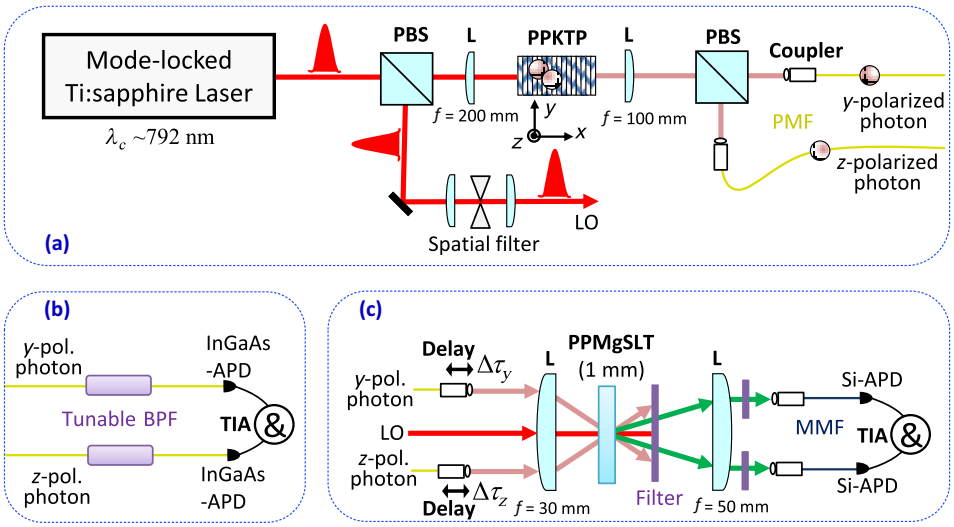

FIG. 4. The experimental setup: (a) how the biphotons are generated; (b) the measurement system for the two-photon spectral intensity (TSI); and (c) the measurement system for the two-photon temporal intensity (TTI). L, lens; PBS, polarizing beam splitter; PMF, polarization maintaining fiber; BPF, bandpass filters; APD, avalanche photodiode; LO, local oscillator; TIA, time-interval analyzer; &, coincidence counter.

ACKNOWLEDGEMENTS

We thank Y. Guo for helpful discussions. R.J. is supported by a fund from the Educational Department of Hubei Province, China (Grant No. D20161504), and by the National Natural Science Foundations of China (Grant No. 11704290). R.S. acknowledges support from the Research Foundation for Opto-Science and Technology, Hamamatsu, Japan, and support from the Matsuo Foundation, Tokyo, Japan.

Note added.—Recently, we noticed that a related work was published [40].

APPENDIX

1. Schematic illustration of the whole experimental setup

The experimental setup is shown in Fig. 4. We use femtosecond laser pulses with a repetition rate of 76 MHz from a mode-locked titanium-sapphire laser, operating at a center wavelength of 792 nm with a bandwidth of 8.1 nm. These are divided into two paths by a polarization beam splitter (PBS) in order to generate and detect biphotons. For the biphoton generation, pulses are sent to a periodically poled potassium titanyl phosphate (PPKTP) crystal with a poling period of 46.1 μm for type-II group-velocity-matched spontaneous parametric down-conversion. To manipulate the two-photon spectral distribution, we also prepare the pump pulse with a bandwidth of 2.8 nm (by inserting a bandpass filter), and crystals of 30 and 10 mm in length. Thanks to the group-velocity matching condition with the femtosecond-laser-pulse pumping, we can generate biphotons with positive frequency correlation at a center wavelength of 1584 nm. Since biphotons generated via the type-II phase-matching condition have orthogonal polarizations, the polarization of the constituent photons is aligned along either the crystallographic y or z axis. The constituent photons are separated by a PBS and coupled into two polarization-maintaining fibers (PMF). The other path of the pump laser pulse is spatially filtered, and then used as a local oscillator (LO) for TTI measurement. For TSI measurement [25,32], each constituent photon of the biphoton is sent to tunable bandpass filters (BPFs), which have a Gaussian-shaped filter function with a fixed FWHM of 0.56 nm and a tunable central wavelength from 1560 to 1620 nm, followed by a two-photon detector consisting of two fiber-coupled single-photon detectors and a time-interval analyzer (TIA). The TSI is measured by scanning the central wavelength of the two BPFs with a step length of 0.5 nm, and recording the coincidence counts for each point. For the TTI measurements, we utilize a time-resolved up-conversion detection system with spatial multiplexing [29,33]. A periodically poled MgO-doped stoichiometric lithium tantalate (PPMgSLT) crystal (poling period of 8.5 μm; length 1 mm) under the type-0 phase-matching condition is used for noncollinear sum-frequency generation (1584 nm + 792 nm $\rightarrow$ 528 nm). After filtering the backgrounds, the up-converted photons are detected by two Si avalanche photodiodes (Si-APD), which are connected to a TIA for coincidence counting. The TTI is measured by scanning the temporal delay between the constituent photons and the LO pulse with a step length of 0.13 ps, and we record the coincidence events. The temporal width of the LO pulse is estimated to be approximately 0.12 ps from the bandwidth of the pump pulse. The group-velocity difference between the LO pulse and the photons passing through the PPMgSLT is calculated to be 0.22 ps. We therefore estimate the temporal resolution for one-photon detection with Si-APD to be $0.12 + 0.22 = 0.34$ ps, and for two-photon detection, $0.34 \times \sqrt{2} \approx 0.48$ ps.

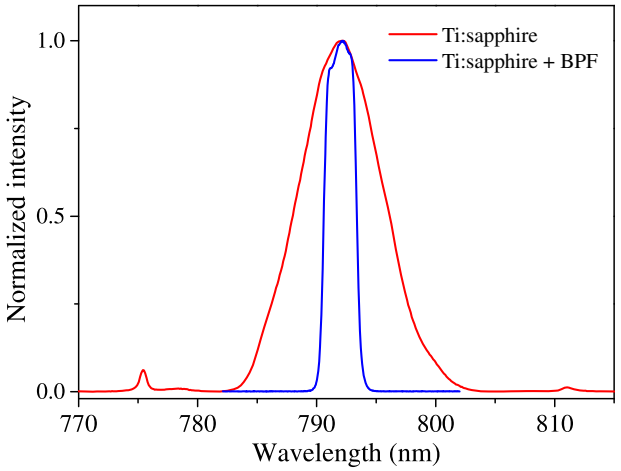

FIG. 5. Pump spectra: (a) red, the original spectrum from the mode-locked titanium sapphire laser; (b) blue, the spectrum after the insertion of a BPF.

2. Pump-pulse spectra for 2.8 and 8.1 nm bandwidths

In our experiment, the femtosecond laser pulse has a Gaussian distribution with a center wavelength of 792 nm and bandwidth of 8.1 nm, as shown in Fig. 5 (red curve). This spectrum is used for the TSIs and TTIs in Figs. 2(b) and 2(c) in the main text. After the insertion of a bandpass filter, the bandwidth becomes 2.8 nm, while the center wavelength is unchanged, as shown in Fig. 5 (blue curve). This spectrum is used for the results in Fig. 2(a) in the main text.

3. Coordinates and parameters

We summarize the coordinates and parameters used in this paper, as shown in Figs. 6(a)–6(f). $\Delta\nu_y$, $\Delta\nu_z$, ν_+, and ν_- are the horizontal, vertical, diagonal, and antidiagonal axes, respectively, in the frequency domain; $\Delta\tau_y$, $\Delta\tau_z$, τ_+, and τ_- are the horizontal, vertical, diagonal, and antidiagonal axes, respectively, in the time domain; $\delta\nu_{yc}$ is the FWHM for the distribution long cross section of $\Delta\nu_z = 0$; meanwhile, $\delta\nu_y$, $\delta\nu_+$, and $\delta\nu_-$ are the FWHM values for the marginal distribution by projecting the data onto the axes of $\Delta\nu_y$, ν_+, and ν_-, respectively. Finally, $\delta\tau_{yc}$ is the FWHM value for the distribution along the cross section of $\Delta\tau_z = 0$; and $\delta\tau_y$, $\delta\tau_+$, and $\delta\tau_-$ are the FWHM values for the marginal distribution by projecting the data onto the axes of $\Delta\tau_y$, τ_+, and τ_-, respectively.

4. Reproduction of the TSIs and TTIs

We take Fig. 2(b) in the main text as an example to show the details of the experimental data-processing method. The image on the left in Fig. 2(b) is the density plot of the TSI, which is scanned along the $\Delta\nu_y$ direction at each $\Delta\nu_z$ value. Figure 7(a) is the waterfall plot of Fig. 2(b). We fit the distributions along the $\Delta\nu_z$ direction using Gaussian functions, and obtain an averaged FWHM value of $\delta\nu_{yc} = 0.21$ THz. Next, we project the TSI data onto the axis of $\Delta\nu_y$, and obtain the marginal distribution, shown in Fig. 3(b). The FWHM value of $\delta\nu_y = 1.9$ THz is estimated using a Gaussian function. Similar results can also be obtained for the temporal data. The density plot of the TTI in Fig. 2(b) is scanned by 76×76 steps. Figure 7(b) is the waterfall plot of the TTI. We fit the distributions along the $\Delta\tau_z$ direction using Gaussian functions, and obtain a FWHM value of $\delta\tau_{yc} = 0.26$ ps. From the projection of the TTI onto the $\Delta\tau_y$ axis, we obtain the marginal distribution, as shown in Fig. 3(b). With a rectangular-like profile, we estimate a FWHM value of $\delta\tau_y = 4.3$ ps. The other four data measurements in Figs. 2(a) and 2(c) are processed

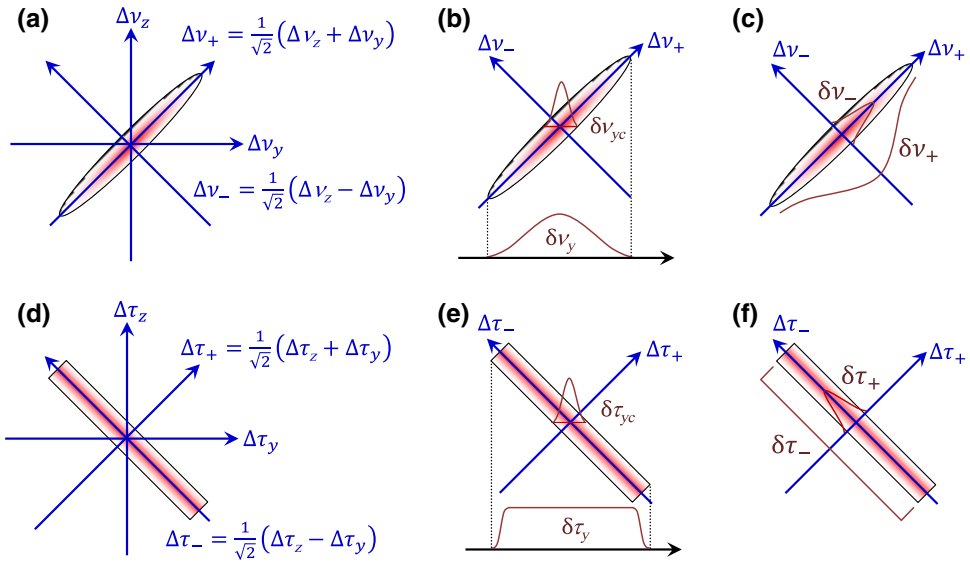

FIG. 6. Coordinates and parameters. (a) The coordinates for the frequency domain. (b) $\delta\nu_{yc}$ is the FWHM of the distribution along the $\Delta\nu_y$ direction; $\delta\nu_y$ is the FWHM of the projected distribution onto the $\Delta\nu_y$ direction. (c) $\delta\nu_+$ is the FWHM of the projected distribution onto the ν_+ direction; $\delta\nu_-$ is the FWHM of the projected distribution onto the ν_- direction. (d) The coordinates for the time domain. (e) $\delta\tau_{yc}$ is the FWHM of the distribution along the $\Delta\tau_y$ direction; $\delta\tau_y$ is the FWHM of the projected distribution onto the $\Delta\tau_y$ direction. (f) $\delta\tau_+$ is the FWHM of the projected distribution onto the τ_+ direction; $\delta\tau_-$ is the FWHM of the projected distribution onto the τ_- direction.

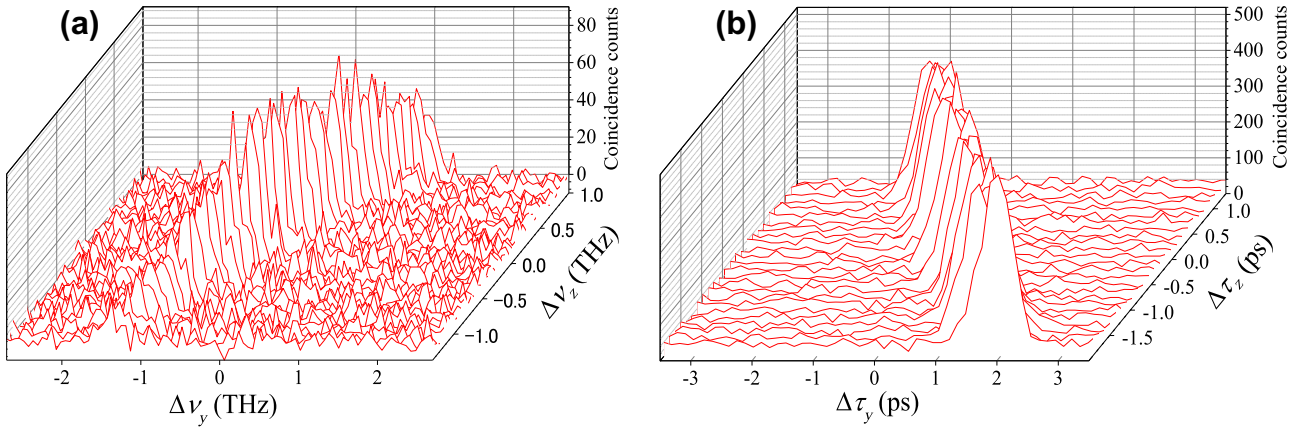

FIG. 7. Detailed analysis of the TSI and TTI: (a) the waterfall plots of the TSI; (b) the TTI in Fig. 2(b).

similarly. Using all the FWHM values, we reproduce the TSIs and TTIs in Fig. 2. We summarize the parameters for the TSI and the TTI in Table II.

5. Measurement of TSI

The TSI is measured using two center-wavelength-tunable BPFs, which have a Gaussian-shaped filter function with a FWHM value of 0.56 nm and a tunable central wavelength from 1560 to 1620 nm [25,32,41]. The single-photon detectors used in this measurement are two InGaAs avalanche photodiode (APD) detectors (ID210, idQuantique), which have a quantum efficiency of around 20%, with a dark count of around 2 kHz. To measure the TSI of the photon pairs, we scan the central wavelength of the two BPFs, and record the coincidence counts. The two BPFs are moved 0.1 nm per step and 60×60 steps in all. The coincidence counts are accumulated for 5 s for each point.

6. Theoretical model of TSI and TTI

For a deeper understanding of this experiment, we construct a simple but effective mathematical model for the biphotons from the PPKTP crystal. The two-photon spectral amplitude (TSA), $f(\nu_s, \nu_i)$, is the product of the pump-envelope function and the phase-matching function. For simplicity in the calculation, we define $\nu_s \equiv \Delta\nu_y$ and $\nu_i \equiv \Delta\nu_y$ as the shifted frequencies of the signal and idler photons in the main text. Without loss of generality, we assume the pump-envelope function as $\alpha(\nu_s + \nu_i) = \exp[-a(\nu_s + \nu_i)^2]$, where a is determined by the spectral width of the pump laser. $\alpha(\nu_s + \nu_i)$ has a distribution at 135° to the horizontal axis [i.e., it is distributed along the antidiagonal direction, as shown in Fig. 8(a)]. The phase-matching function is $\Phi(\omega_s, \omega_i) = \mathrm{sinc}[b(\nu_s - \nu_i)]$, where b is determined by the length of the PPKTP crystal. The PPKTP crystal satisfies the group-velocity-matching (GVM) condition at telecom wavelengths [14,31,32,42,43]; therefore, its phase-matching function has a distribution at 45° to the horizontal axis [i.e., distributed along the diagonal direction, as shown in Fig. 8(b)]. The TSA can be written as $f(\nu_s, \nu_i) = \exp[-a(\nu_s + \nu_i)^2]\mathrm{sinc}[b(\nu_s - \nu_i)]$, which is the product of the pump-envelope function and the phase-matching function. In this experiment, the pump envelope is wider than the phase-matching function; therefore, their product is also distributed along the diagonal direction. That is, the signal and idler are positively correlated, as shown in Fig. 8(c). The two-photon spectral intensity is $|f(\nu_s, \nu_i)|^2$, as shown in Fig. 8(d). After the long calculation described in Eq. (A2), the Fourier transform of $f(\nu_s, \nu_i)$ can be analytically obtained as $F(t_s, t_i) = c_0 \exp[-(t_s + t_i)^2/16a]\,\mathrm{rect}[(t_s - t_i)/2b]$, where $c_0 = 2\pi^3\sqrt{\pi}/(b\sqrt{a})$. Note that we define $t_s \equiv \Delta\tau_y$ and $t_i \equiv \Delta\tau_z$ as the shifted times for the signal and idler photons in the main text. Here, $\exp[-(t_s + t_i)^2/16a]$ is the pump-envelope function in the time domain; $\mathrm{rect}[(t_s - t_i)/2b]$ is the phase-matching function in the time domain; $F(t_s, t_i)$ is the two-photon temporal amplitude (TSA); and $|F(t_s, t_i)|^2$ is just the two-photon

TABLE II. The parameters for the TSI and the TTI: a summary of the bandwidths for measured and reproduced TSI and TTI.

	Width		Measured				Reproduced			
	Unit		$\delta\nu_y$	$\delta\nu_{yc}$	$\delta\tau_y$	$\delta\tau_{yc}$	$\delta\nu_+$	$\delta\nu_-$	$\delta\tau_+$	$\delta\tau_-$
a	$\Delta\lambda_p = 2.8$ nm	$L = 30$ mm	0.82	0.19	4.2	0.54	1.2	0.13	0.38	5.9
b	$\Delta\lambda_p = 8.1$ nm	$L = 30$ mm	1.9	0.21	4.3	0.26	2.7	0.14	0.18	6.1
c	$\Delta\lambda_p = 8.1$ nm	$L = 10$ mm	1.7	0.49	1.3	0.25	2.3	0.33	0.18	1.8

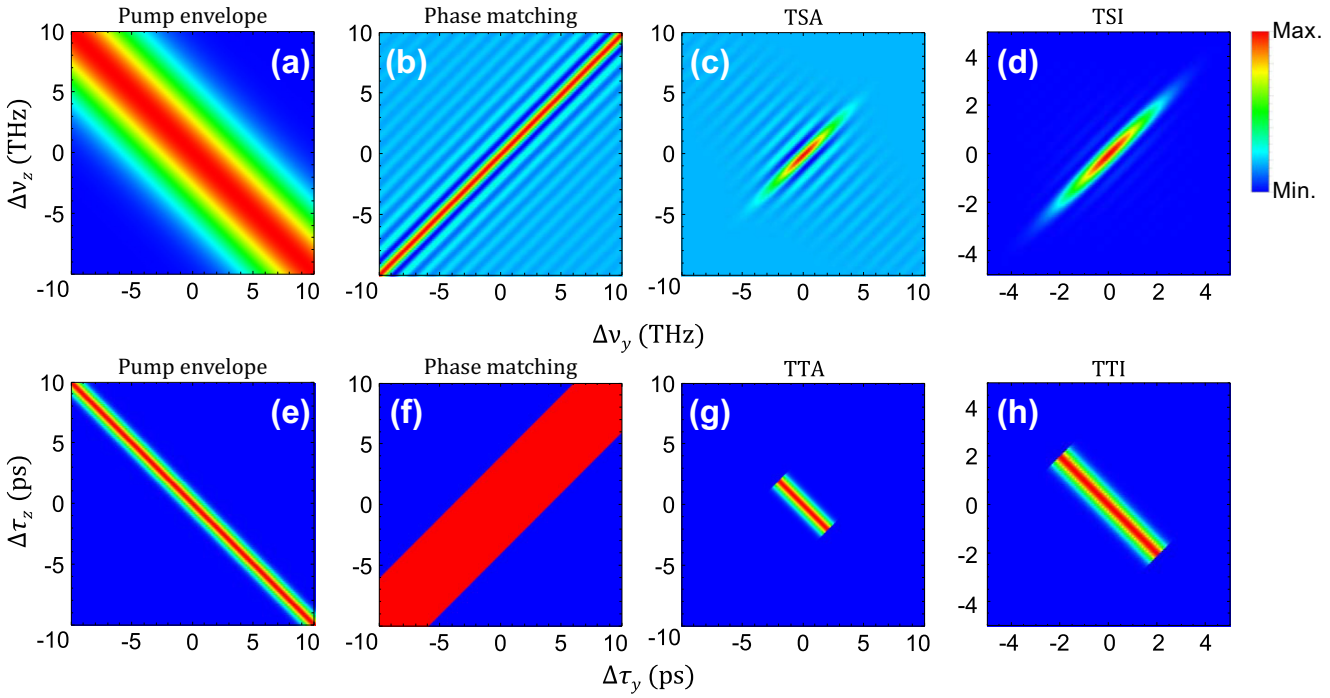

FIG. 8. The mathematical model. The top row is for the spectral distribution: (a) the pump envelope function $\exp[-a(\nu_s+\nu_i)^2]$; (b) the phase-matching function $\mathrm{sinc}[b(\nu_s-\nu_i)]$; (c) the two-photon spectral amplitude (TSA) $f(\nu_s,\nu_i)$; (d) the two-photon spectral intensity (TSI) $|f(\nu_s,\nu_i)|^2$. The bottom row shows the corresponding temporal distributions: (e) the temporal pump envelope function $\exp[-(t_s+t_i)^2/16a]$; (f) the temporal phase-matching function $\mathrm{rect}[(t_s-t_i)/2b]$; (g) the two-photon temporal amplitude (TTA) $F(t_s,t_i)$; (h) the two-photon temporal intensity (TTI) $|F(t_s,t_i)|^2$. The parameters are set at $a=0.04$ and $b=4$ for all the figures.

temporal intensity (TTI). The distribution of these functions is shown in Figs. 8(e)–8(h). It is interesting to note that ν_s and ν_i cannot be written in a separated form in $f(\nu_s,\nu_i)$. However, if we introduce new variables $\nu_\pm=\frac{1}{\sqrt{2}}(\nu_s\pm\nu_i)$, ν_+ and ν_- can be separated in $f(\nu_+,\nu_-)$. The situation is similar for τ_s and τ_i, as explained in Eq. (3) in the main text. Another interesting feature is that the pump-envelope and phase-matching functions are independent from each other in both the spectral and temporal domains. The spectral and temporal phase-matching functions are varied simultaneously by changing the parameter a, while the phase-matching functions are not affected. Similar phenomena can be observed for the spectral and temporal pump-envelope functions by changing the parameter b: varying the *sinc* function in the spectral domain corresponds to varying the *rect* function in the time domain, while the Gaussian-shaped spectral and temporal pump-envelope functions are not affected.

This model is used for the simulations of Fig. 2 in the main text. For Fig. 2(a), we change the pump-envelope function from a Gaussian function to a convolution between a Gaussian function and a rectangular function, because the pump laser for Fig. 2(a) is filtered by a near-rectangular-shaped BPF.

7. Theoretical calculation of TTA from TSA

For a pump-envelope function $\exp[-a(\nu_s+\nu_i)^2]$ and a phase-matching function $\mathrm{sinc}[b(\nu_s-\nu_i)]$, the two-photon spectral amplitude (TSA) can be written as

$$f(\nu_s,\nu_i)=\exp[-a(\nu_s+\nu_i)^2]\mathrm{sinc}[b(\nu_s-\nu_i)]. \quad \text{(A1)}$$

The two-photon temporal amplitude (TTA) is the Fourier transform ($\mathscr{F}$) of $f(\nu_s,\nu_i)$, and can be calculated as follows:

$$\begin{aligned}
&\mathscr{F}\{f(\nu_s,\nu_i)\}\\
&=\mathscr{F}\{\exp[-a(\nu_s+\nu_2)^2]\,\mathrm{sinc}[b(\nu_s-\nu_2)]\}\\
&=\mathscr{F}\{\exp[-a(\nu_s+\nu_i)^2]\}\otimes\mathscr{F}\{\mathrm{sinc}[b(\nu_s-\nu_i)]\}\\
&=\left[2\pi\sqrt{\frac{\pi}{a}}\exp\left(-\frac{t_s^2}{4a}\right)\delta(t_s-t_i)\right]\\
&\quad\otimes\left[2\pi^2\frac{1}{b}\,\mathrm{rect}\left(\frac{t_s}{b}\right)\delta(t_s+t_i)\right]\\
&=\int_{-\infty}^{\infty}\int_{-\infty}^{\infty}d\tau_s d\tau_i\left[2\pi\sqrt{\frac{\pi}{a}}\exp\left(-\frac{\tau_s^2}{4a}\right)\delta(\tau_s-\tau_i)\right]\\
&\quad\left[2\pi^2\frac{1}{b}\,\mathrm{rect}\left(\frac{t_s-\tau_s}{b}\right)\delta(t_s+t_i-\tau_s-\tau_i)\right]
\end{aligned}$$

$$
\begin{aligned}
&= \int_{-\infty}^{\infty} d\tau_s \left[2\pi \sqrt{\frac{\pi}{a}} \exp\left(-\frac{\tau_s^2}{4a} \right) \right] \\
&\quad \left[2\pi^2 \frac{1}{b} \mathrm{rect}\left(\frac{t_s - \tau_s}{b} \right) \delta(t_s + t_i - \tau_s - \tau_s) \right] \\
&= \int_{-\infty}^{\infty} d\tau_s \left[2\pi \sqrt{\frac{\pi}{a}} \exp\left(-\frac{\tau_s^2}{4a} \right) \right] \\
&\quad \left[2\pi^2 \frac{1}{b} \mathrm{rect}\left(\frac{t_s - \tau_s}{b} \right) \frac{1}{2} \delta\left(\tau_s - \frac{t_s + t_i}{2} \right) \right] \\
&= \frac{2\pi^3}{b} \sqrt{\frac{\pi}{a}} \exp\left[-\frac{(t_s + t_i)^2}{16a} \right] \mathrm{rect}\left(\frac{t_s - t_i}{2b} \right) \\
&= c_0 \exp\left[-\frac{(t_s + t_i)^2}{16a} \right] \mathrm{rect}\left(\frac{t_s - t_i}{2b} \right), \qquad \text{(A2)}
\end{aligned}
$$

where $\otimes$ is the convolution symbol and $c_0 = 2\pi^3\sqrt{\pi}/(b\sqrt{a})$. In conclusion, the TTA ($F(t_s, t_i)$) can be calculated from the Fourier transform of TSA ($f(\nu_s, \nu_i)$), with the following form:

$$
\begin{aligned}
F(t_s, t_i) &= \mathscr{F}\{f(\nu_s, \nu_i)\} \\
&= c_0 \exp\left[-\frac{(t_s + t_i)^2}{16a} \right] \mathrm{rect}\left(\frac{t_s - t_i}{2b} \right). \qquad \text{(A3)}
\end{aligned}
$$

[1] H. Stark, *Applications of optical Fourier transforms* (Academic Press, Orlando, FL, 1982).

[2] J. W. Goodman, *Introduction to Fourier Optics* (W. H. Freeman, New York, 2017), 4th ed.

[3] C. Zhang, X. Wei, M. E. Marhic, and K. K. Y. Wong, Ultrafast and versatile spectroscopy by temporal Fourier transform, Sci. Rep. **4**, 5351 (2014).

[4] B. C. Smith, *Fundamentals of Fourier Transform Infrared Spectroscopy* (CRC Press, Boca Raton, FL, 2011), 2nd ed.

[5] R. Bell, *Introductory Fourier Transform Spectroscopy* (Academic Press, New York, 1972), 1st ed.

[6] R. Sirohi, *Optical Methods of Measurement: Whole Field Techniques* (CRC Press, Boca Raton, FL, 2017), 2nd ed.

[7] P. R. Griffiths and J. A. De Haseth, *Fourier Transform Infrared Spectrometry* (Wiley-Interscience, Hoboken, NJ, 2007), 2nd ed.

[8] A. VanderLugt, *Optical Signal Processing* (Wiley-Interscience, Hoboken, NJ, 2005).

[9] W. Rhodes, *Fourier Optics and Optical Signal Processing* (Wiley-Blackwell, Hoboken, NJ, 2009).

[10] H.-S. Chan, Z.-M. Hsieh, W.-H. Liang, A. H. Kung, C.-K. Lee, C.-J. Lai, R.-P. Pan, and L.-H. Peng, Synthesis and measurement of ultrafast waveforms from five discrete optical harmonics, Science **331**, 1165 (2011).

[11] N. S. Suhaimi, C. Ohae, T. Gavara, K. Nakagawa, F.-L. Hong, and M. Katsuragawa, Generation of five phase-locked harmonics by implementing a divide-by-three optical frequency divider, Opt. Lett. **40**, 5802 (2015).

[12] S. Kocsis, B. Braverman, S. Ravets, M. J. Stevens, R. P. Mirin, L. K. Shalm, and A. M. Steinberg, Observing the average trajectories of single photons in a two-slit interferometer, Science **332**, 1170 (2011).

[13] R. S. Aspden, M. J. Padgett, and G. C. Spalding, Video recording true single-photon double-slit interference, Am. J. Phys. **84**, 671 (2016).

[14] A. Eckstein, A. Christ, P. J. Mosley, and C. Silberhorn, Highly Efficient Single-Pass Source of Pulsed Single-Mode Twin Beams of Light, Phys. Rev. Lett. **106**, 013603 (2011).

[15] R.-B. Jin, R. Shimizu, M. Fujiwara, M. Takeoka, R. Wakabayashi, T. Yamashita, S. Miki, H. Terai, T. Gerrits, and M. Sasaki, Simple method of generating and distributing frequency-entangled qudits, Quantum Sci. Technol. **1**, 015004 (2016).

[16] C. Chen, C. Bo, M. Y. Niu, F. Xu, Z. Zhang, J. H. Shapiro, and F. N. C. Wong, Efficient generation and characterization of spectrally factorable biphotons, Opt. Express **25**, 7300 (2017).

[17] R.-B. Jin, G.-Q. Chen, H. Jing, C. Ren, P. Zhao, R. Shimizu, and P.-X. Lu, Monotonic quantum-to-classical transition enabled by positively correlated biphotons, Phys. Rev. A **95**, 062341 (2017).

[18] D. C. Burnham and D. L. Weinberg, Observation of Simultaneity in Parametric Production of Optical Photon Pairs, Phys. Rev. Lett. **25**, 84 (1970).

[19] C. K. Hong, Z. Y. Ou, and L. Mandel, Measurement of Subpicosecond Time Intervals Between Two Photons by Interference, Phys. Rev. Lett. **59**, 2044 (1987).

[20] T. S. Larchuk, R. A. Campos, J. G. Rarity, P. R. Tapster, E. Jakeman, B. E. A. Saleh, and M. C. Teich, Interfering Entangled Photons of Different Colors, Phys. Rev. Lett. **70**, 1603 (1993).

[21] Y. H. Shih, A. V. Sergienko, M. H. Rubin, T. E. Kiess, and C. O. Alley, Two-photon interference in a standard Mach-Zehnder interferometer, Phys. Rev. A **49**, 4243 (1994).

[22] V. Giovannetti, L. Maccone, J. H. Shapiro, and F. N. C. Wong, Generating Entangled Two-Photon States with Coincident Frequencies, Phys. Rev. Lett. **88**, 183602 (2002).

[23] R.-B. Jin and R. Shimizu, Extended Wiener-Khinchin theorem for quantum spectral analysis, Optica **5**, 93 (2018).

[24] Y.-H. Kim and W. P. Grice, Measurement of the spectral properties of the two-photon state generated via type II spontaneous parametric downconversion, Opt. Lett. **30**, 908 (2005).

[25] R. Shimizu and K. Edamatsu, High-flux and broadband biphoton sources with controlled frequency entanglement, Opt. Express **17**, 16385 (2009).

[26] M. Avenhaus, A. Eckstein, P. J. Mosley, and C. Silberhorn, Fiber-assisted single-photon spectrograph, Opt. Lett. **34**, 2873 (2009).

[27] B. Fang, O. Cohen, M. Liscidini, J. E. Sipe, and V. O. Lorenz, Fast and highly resolved capture of the joint spectral density of photon pairs, Optica **1**, 281 (2014).

[28] M. Allgaier, G. Vigh, V. Ansari, C. Eigner, V. Quiring, R. Ricken, B. Brecht, and C. Silberhorn, arXiv:1702.03240.

[29] O. Kuzucu, F. N. C. Wong, S. Kurimura, and S. Tovstonog, Joint Temporal Density Measurements for Two-Photon

State Characterization, Phys. Rev. Lett. **101**, 153602 (2008).

[30] Y.-W. Cho, K.-K. Park, J.-C. Lee, and Y.-H. Kim, Engineering Frequency-Time Quantum Correlation of Narrow-Band Biphotons from Cold Atoms, Phys. Rev. Lett. **113**, 063602 (2014).

[31] F. König and F. N. C. Wong, Extended phase matching of second-harmonic generation in periodically poled $KTiOPO_4$ with zero group-velocity mismatch, Appl. Phys. Lett. **84**, 1644 (2004).

[32] R.-B. Jin, R. Shimizu, K. Wakui, H. Benichi, and M. Sasaki, Widely tunable single photon source with high purity at telecom wavelength, Opt. Express **21**, 10659 (2013).

[33] O. Kuzucu, F. N. C. Wong, S. Kurimura, and S. Tovstonog, Time-resolved single-photon detection by femtosecond upconversion, Opt. Lett. **33**, 2257 (2008).

[34] M. A. Nielsen and I. L. Chuang, *Quantum Computation and Quantum Information* (Cambridge University Press, Cambridge, 2000).

[35] A. F. Abouraddy, M. B. Nasr, B. E. A. Saleh, A. V. Sergienko, and M. C. Teich, Demonstration of the complementarity of one- and two-photon interference, Phys. Rev. A **63**, 063803 (2001).

[36] R. Shimizu, K. Edamatsu, and T. Itoh, Quantum diffraction and interference of spatially correlated photon pairs and its Fourier-optical analysis, Phys. Rev. A **74**, 013801 (2006).

[37] T. Schweigler, V. Kasper, S. Erne, I. Mazets, B. Rauer, F. Cataldini, T. Langen, T. Gasenzer, J. Berges, and J. Schmiedmayer, Experimental characterization of a quantum many-body system via higher-order correlations, Nature **545**, 323 (2017).

[38] A. J. Menssen, A. E. Jones, B. J. Metcalf, M. C. Tichy, S. Barz, W. S. Kolthammer, and I. A. Walmsley, Distinguishability and Many-Particle Interference, Phys. Rev. Lett. **118**, 153603 (2017).

[39] S. Agne, T. Kauten, J. Jin, E. Meyer-Scott, J. Z. Salvail, D. R. Hamel, K. J. Resch, G. Weihs, and T. Jennewein, Observation of Genuine Three-Photon Interference, Phys. Rev. Lett. **118**, 153602 (2017).

[40] J.-P. W. MacLean, J. M. Donohue, and K. J. Resch, Direct Characterization of Ultrafast Energy-Time Entangled Photon Pairs, Phys. Rev. Lett. **120**, 053601 (2018).

[41] N. S. Bisht and R. Shimizu, Spectral properties of broadband biphotons generated from PPMgSLT under a type-II phase-matching condition, J. Opt. Soc. Am. B **32**, 550 (2015).

[42] P. G. Evans, R. S. Bennink, W. P. Grice, T. S. Humble, and J. Schaake, Bright Source of Spectrally Uncorrelated Polarization-Entangled Photons with Nearly Single-Mode Emission, Phys. Rev. Lett. **105**, 253601 (2010).

[43] T. Gerrits, M. J. Stevens, B. Baek, B. Calkins, A. Lita, S. Glancy, E. Knill, S. W. Nam, R. P. Mirin, R. H. Hadfield, R. S. Bennink, W. P. Grice, S. Dorenbos, T. Zijlstra, T. Klapwijk, and V. Zwiller, Generation of degenerate, factorizable, pulsed squeezed light at telecom wavelengths, Opt. Express **19**, 24434 (2011).